

Vacancy Associates-Rich Ultrathin Nanosheets for High Performance and Flexible Nonvolatile Memory Device

Lin Liang,^{†,||} Kun Li,^{†,||} Chong Xiao,^{*,†} Shaojuan Fan,[‡] Jiao Liu,[†] Wenshuai Zhang,[‡] Wenhui Xu,[†] Wei Tong,[§] Jiaying Liao,[†] Yingying Zhou,[†] Bangjiao Ye,[‡] and Yi Xie^{*,†}

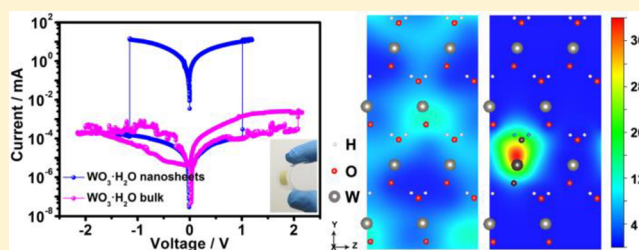
[†]Hefei National Laboratory for Physical Sciences at the Microscale and Collaborative Innovation Center of Chemistry for Energy Materials, University of Science & Technology of China, Hefei, Anhui 230026, P. R. China

[‡]State Key Laboratory of Particle Detection and Electronics, University of Science & Technology of China, Hefei, Anhui 230026, P. R. China

[§]High Magnetic Field Laboratory, Chinese Academy of Sciences, Hefei, Anhui 230031, P.R. China

Supporting Information

ABSTRACT: On the road of innovation in modern information technology, resistive switching random access memory (RRAM) has been considered to be the best potential candidate to replace the conventional Si-based technologies. In fact, the key prerequisite of high storage density and low power consumption as well as flexibility for the tangible next generation of nonvolatile memories has stimulated extensive research into RRAM. Herein, we highlight an inorganic graphene analogue, ultrathin $\text{WO}_3 \cdot \text{H}_2\text{O}$ nanosheets with only 2–3 nm thickness, as a promising material to construct a high performance and flexible RRAM device. The abundant vacancy associates in the ultrathin nanosheets, revealed by the positron annihilation spectra, act not only carrier reservoir to provide carriers but also capture center to trap the actived Cu^{2+} for the formation of conductive filaments, which synergistically realize the resistive switching memory with low operating voltage (+1.0 V/−1.14 V) and large resistance ON/OFF ratio ($>10^5$). This ultrathin-nanosheets-based RRAM device also shows long retention time ($>10^5$ s), good endurance (>5000 cycles), and excellent flexibility. The finding of the existence of distinct defects in ultrathin nanosheets undoubtedly leads to an atomic level deep understanding of the underlying nature of the resistive switching behavior, which may serve as a guide to improve the performances and promote the rapid development of RRAM.



INTRODUCTION

The road of innovation in modern information technology has stimulated extensive research into the development of non-volatile memory (NVM) technologies to replace the conventional Si-based technologies.^{1–3} Among the many competitors for NVM, resistive switching random access memory (RRAM) has attracted the most considerable attention thanks to its superiority of simple structure, high-density integration, low power consumption, and good compatibility.^{4–8} However, to achieve these superiorities in practical devices is strongly dependent on the robust and predictive understanding of resistive switching mechanism, especially on the atomic level.^{9–11} Although many mechanisms have been proposed to investigate the resistive switching processes, it is still a contentious issue because of their uncertainty in different materials systems. Thus, providing an applicable model not only fills an urgent need that enables accurate simulation of large-scale memristor systems but also can significantly improve our understanding of the different factors that drive the switching process, which will be critical for continued optimization and design of this important class of devices.

On the other hand, a typical RRAM device is usually built in a two-terminal metal/insulator (or semiconductor)/metal configuration, where the insulator/semiconductor acts as the active layer for resistive switching. From this perspective, exploring flexible RRAM devices in an all solid state, offering great advantages of being lightweight, printable, foldable, and stretchable, has become a central issue in the field of information technology.^{12–16} Although several recent studies have reported the fabrication of flexible RRAM devices, significant challenges remain in this area from the fundamental limits of conventional materials, both including bulk and nanoparticles, because the poor adhesion between materials and substrates usually results in cracking and detachment under repetitive bending or strain conditions. In fact, the endurance of the flexible RRAM device in a variety of environments has become a major and urgent obstacle. Fortunately, the emergence of two-dimensional (2D) atomically ultrathin nanosheets with unique electronic structures and physical properties, such as graphene and its analogues, brings a new

Received: January 2, 2015

Published: February 10, 2015

dawn for the development of flexible electronic devices.^{17–19} As well as its peculiar electrical properties, 2D materials often demonstrate a significant Young's modulus and breaking strength. Thus, it is reasonable to suggest that 2D ultrathin nanosheets may be attractive solutions for flexible electronics. In fact, 2D ultrathin nanosheets have attracted considerable attentions as an ideal material platform for constructing flexible electronic devices during the past years.

As one of the most ideal candidates for future RRAM,^{2,20,21} tungsten oxides (WO_3) have been intensively investigated because they have potential advantages such as simple composition, easy fabrication, and high compatibility with the back-end-line process in the complementary metal-oxide-semiconductor (CMOS) technology. Of note, as important polytype structure of tungsten oxide, the hydrated tungsten oxides ($\text{WO}_3 \cdot n\text{H}_2\text{O}$) usually possess layered structure, which can be easily exfoliated into ultrathin nanosheets through simple wet chemical method. For example, in the layered $\text{WO}_3 \cdot 2\text{H}_2\text{O}$,^{22,23} half of water locates between the $\text{WO}_3[\text{H}_2\text{O}]$ layers, which is composed of distorted $\text{WO}_5(\text{H}_2\text{O})$ octahedrons in corner-sharing mode. This existence of interlaminar water can increase the distance between adjacent layers to supply a larger spacing, which makes $\text{WO}_3 \cdot 2\text{H}_2\text{O}$ facily exfoliate into 2D nanosheets. Although the hydrated tungsten oxide layered structure shows the prospective signs in thin flexible devices, the in-depth investigation of these promising materials in the emerging field of flexible RRAM devices is still scarcity.

Herein, we highlight a flexible nonvolatile memory device based on ultrathin $\text{WO}_3 \cdot \text{H}_2\text{O}$ nanosheets, which features low set/reset voltages, a larger ON/OFF ratio, long retention time, and good endurance. The 2D ultrathin characteristic of $\text{WO}_3 \cdot \text{H}_2\text{O}$ nanosheets endows this device excellent flexibility. Experimental results establish that the high performance of this device is mediated by a dual synergic mechanism. Memristive electrical switching proceeds by means of the carriers release and activated Cu^{2+} drift through the vacancy associates. The current findings definitely contribute further understanding of complex RS mechanisms and promote the development of the high performance and flexible RRAM devices.

■ EXPERIMENTAL SECTION

Synthesis of Bulk $\text{WO}_3 \cdot 2\text{H}_2\text{O}$. In a typical experiment, 400 mg of $\text{Na}_2\text{WO}_4 \cdot 2\text{H}_2\text{O}$ were dispersed in 300 mL of 4.8 M nitric acid solution. The mixture was stirred for 72 h at 20 °C. The obtained light yellow precipitates were separated by centrifuging and washed with deionized water for several times. Finally, the powdery products were dried overnight at room temperature.

Liquid-Exfoliation of Bulk $\text{WO}_3 \cdot 2\text{H}_2\text{O}$. In our experiment, 10 mg of bulk $\text{WO}_3 \cdot 2\text{H}_2\text{O}$ were dispersed in 10 mL of DMF and then ultrasonicated in ice water for 3 h. A light yellow suspension was obtained and centrifuged at 5000 rpm for 10 min to remove the nonexfoliated component. After centrifugation, the supernatant was collected by centrifuging at 13 000 rpm for 5 min and then washed with deionized water once. The obtained $\text{WO}_3 \cdot \text{H}_2\text{O}$ ultrathin nanosheets were redispersed in water.

Fabrication of Flexible RRAM Device. Poly(ethylene terephthalate) (PET) coated with indium tin oxide (ITO) was employed as the flexible substrate and purchased from Sigma-Aldrich (45 Ω/sq). PET and ITO were used as substrate and bottom electrode, respectively. The fabrication process for the

films was shown as follows: First, the dispersion of $\text{WO}_3 \cdot \text{H}_2\text{O}$ ultrathin nanosheets was vacuum filtrated onto a cellulose membrane with a 0.22 μm pore size, forming a light-yellow homogeneous thin film. The thickness of the film can be readily controlled by tuning volume and concentration of the filtrated solution. Second, the obtained $\text{WO}_3 \cdot \text{H}_2\text{O}$ thin film on cellulose membrane was pressed onto the ITO/PET sheet with the assistance of small amount of ethanol. Then, the film on the ITO/PET sheet was immersed in acetone to gradually dissolved the cellulose membrane. After an hour, the acetone was aspirated and the film was reimmersed with fresh acetone again. As a result, $\text{WO}_3 \cdot \text{H}_2\text{O}$ ultrathin nanosheets-based film with a 1 cm \times 1 cm planar size was successfully transferred onto flexible ITO/PET sheet with a size of 2 cm \times 4 cm. Finally, copper network was used as the top electrode, which was pressed closely on the nanosheets-based film deposited on ITO/PET sheet.

Characterization. X-ray diffraction (XRD) was recorded on a Philips X'Pert Pro Super diffractometer with $\text{Cu K}\alpha$ radiation ($\lambda = 1.54178 \text{ \AA}$). The field emission scanning electron microscopy (FE-SEM) images were taken on a JEOL JSM-6700F SEM. The transmission electron microscopy (TEM) images and high-resolution TEM (HRTEM) images were performed on a JEOL-2010 transmission electron microscope at an acceleration voltage of 200 kV. Tapping-mode atomic force microscopy (AFM) images were carried out on DI Innova Multimode SPM platform.

Positron Annihilation Measurement. To perform the positron lifetime experiments, the as-prepared samples were pressed into round disc with thickness of 1 mm, and then a 5 mCi source of ^{22}Na was sandwiched between two pressed identical samples. The positron lifetime experiments were carried out with a fast-slow coincidence ORTEC system with a time resolution of about 230 ps full width at half-maximum. The lifetime of a positron in a perfect bulk crystal or that of a positron trapped at a defect were calculated by solving the three-dimensional Kohn–Sham equation with the finite-difference method based on the conventional scheme.²⁴ To obtain the electron density and the Coulomb potential, several self-consistent calculations for electronic-structures were performed with the PBE-GGA approach²⁵ for electron–electron exchange–correlations. For finally getting the positron lifetimes, the GGA (generalized gradient approximation) form of the enhancement factor proposed by Barbiellini²⁶ was chosen. In addition, the unrelaxed $2 \times 2 \times 2$ supercell was adopted for calculating the lifetime for the positron trapped at a defect.

Electrical Switching Measurement. The resistive switching behavior of the as-fabricated RRAM devices were measured using an electrochemical station (CHI 660B) with a sweeping voltage applied to the top electrode. The device endurance was recorded during each voltage sweeping at a read out voltage of 0.1 V. The measurement conditions were kept consistent for nanosheets- and bulk-based devices. For the flexibility test, the devices were repeatedly bended with bending radius of 8 mm and 1.2 cm for nanosheets-based and bulk-based devices, respectively.

■ RESULTS AND DISCUSSION

In this study, the free-standing $\text{WO}_3 \cdot \text{H}_2\text{O}$ ultrathin nanosheets were successfully synthesized via ultrasonic exfoliation of bulk $\text{WO}_3 \cdot 2\text{H}_2\text{O}$ in DMF (details experiment as seen in the methods, and the correspond XRD pattern and SEM image

of this bulk $\text{WO}_3 \cdot 2\text{H}_2\text{O}$ seen in Supporting Information Figure S1). As shown in Figure 1a (orange line), the sole strong

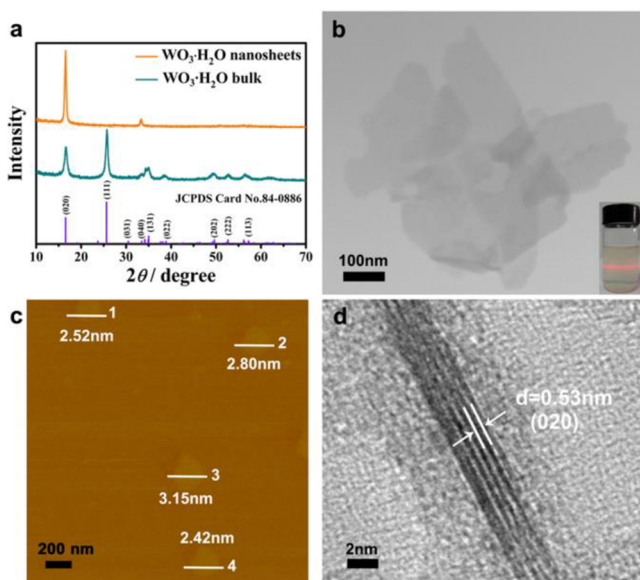


Figure 1. (a) XRD pattern of $\text{WO}_3 \cdot \text{H}_2\text{O}$ ultrathin nanosheets-based film, the violet lines give the corresponding standard pattern of JCPDS Card No. 84–0886. (b) TEM image of $\text{WO}_3 \cdot \text{H}_2\text{O}$ ultrathin nanosheets and the corresponding colloidal dispersion displaying the Tyndall effect (inset). (c) AFM image and height profiles of $\text{WO}_3 \cdot \text{H}_2\text{O}$ ultrathin nanosheets. (d) Cross-sectional TEM image of $\text{WO}_3 \cdot \text{H}_2\text{O}$ ultrathin nanosheets.

diffraction peak of corresponding XRD pattern of the as-obtained $\text{WO}_3 \cdot \text{H}_2\text{O}$ ultrathin nanosheets-based film fabricated by a layer-by-layer assembly strategy could be well indexed to the (020) facet of orthorhombic $\text{WO}_3 \cdot \text{H}_2\text{O}$ (JCPDS No. 84-0886), whereas the other small diffraction peak could be assigned to the (040) facet. This reasonably indicates a highly preferred (010) orientation in the nanosheets, which is further verified by the corresponding high-resolution transmission electron microscopy (HRTEM) image and the selected-area electron diffraction (SAED) pattern as shown in Supporting Information Figure S2. For comparison, the XRD pattern of $\text{WO}_3 \cdot \text{H}_2\text{O}$ bulk is depicted in the green line of Figure 1a, which can be readily indexed to orthorhombic $\text{WO}_3 \cdot \text{H}_2\text{O}$ without apparent orientation. The transmission electron microscopy (TEM) image of the exfoliated product shown in Figure 1b clearly reveals sheetlike morphology with lateral size larger than 300 nm, and its near transparency shows the ultrathin thickness. Macroscopically, the colloidal suspension of $\text{WO}_3 \cdot \text{H}_2\text{O}$ ultrathin nanosheets was very stable over one month and displayed Tyndall effect (inset of Figure 1b), inferring the presence of highly monodisperse ultrathin nanosheets in DMF. As depicted in Figure 2c and Supporting Information Figure S3, the atomic force microscopy (AFM) image and their corresponding height distribution show the smooth 2D sheets with about 2–3 nm thickness, matching well with 4-fold or 5-fold interlayer distance of 0.53 nm between adjacent $\text{WO}_3[\text{H}_2\text{O}]$ layers along the [010] direction, which is consistent with the result from the TEM measurement of the folded edge of a nanosheet (Figure 1d).

A resistive switching random access memory device consisting of $\text{Cu}/\text{WO}_3 \cdot \text{H}_2\text{O}/\text{ITO-PET}$ is schematically illustrated in Figure 2a (for details see Experimental Section). For

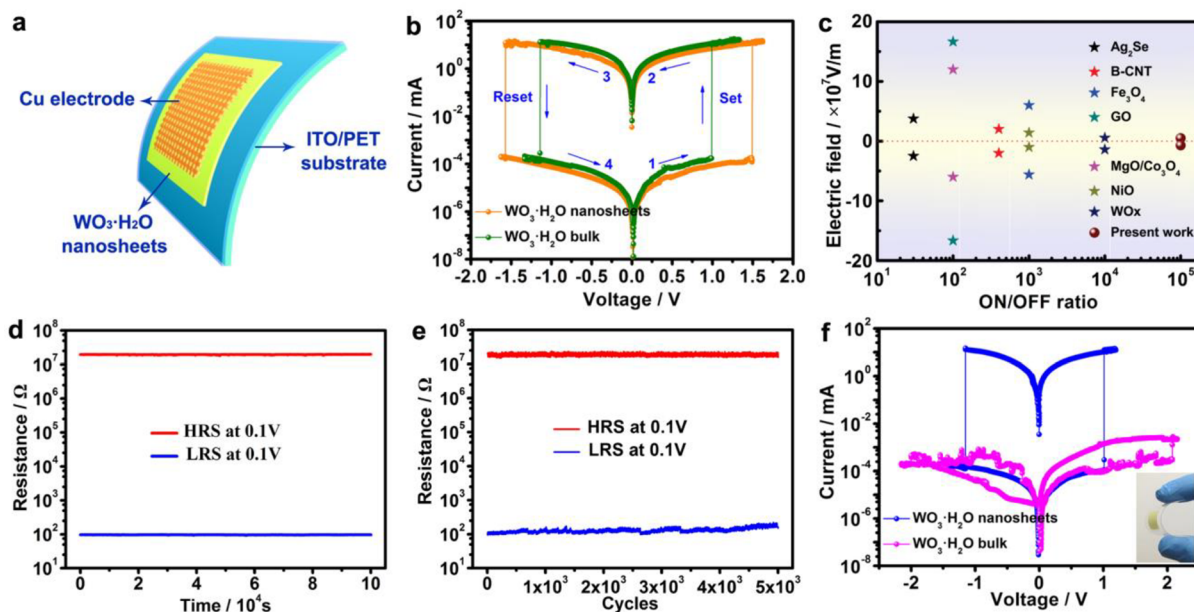


Figure 2. (a) Schematic illustration of flexible RRAM device with a $\text{Cu}/\text{WO}_3 \cdot \text{H}_2\text{O}/\text{ITO-PET}$ configuration. (b) Current versus voltage (I – V) curves of the ultrathin $\text{WO}_3 \cdot \text{H}_2\text{O}$ nanosheets-based and bulk-based RRAM devices at initial cycle. The arrows and numbers indicate the voltage sweep directions. (c) Our RRAM device based on ultrathin $\text{WO}_3 \cdot \text{H}_2\text{O}$ nanosheets showing much better performance of set/reset voltage and ON/OFF ratio compared with most of the reported typical resistive switching inorganic materials, such as WO_x ,²¹ NiO ,²⁷ Ag_2Se ,¹⁵ Fe_3O_4 ,²⁸ B-CNT ,²⁹ GO ,³⁰ $\text{MgO}/\text{Co}_3\text{O}_4$.³¹ (d) Retention of the $\text{WO}_3 \cdot \text{H}_2\text{O}$ nanosheets-based RRAM devices. (e) Endurance performance of the $\text{WO}_3 \cdot \text{H}_2\text{O}$ nanosheets-based RRAM devices. (f) I – V curves obtained from the $\text{WO}_3 \cdot \text{H}_2\text{O}$ nanosheets-based and bulk-based RRAM devices after 2000 and 100 bending tests, respectively. Inset is a digital photograph of a bent RRAM device with a bending radius of 8 mm and 1.2 cm for nanosheets-based and bulk-based devices, respectively.

comparison, we adopted $\text{WO}_3\cdot\text{H}_2\text{O}$ ultrathin nanosheets and bulk as the active layer, respectively. The cross-section SEM image of the ultrathin nanosheets-based device (as shown in the Supporting Information Figure S4) clearly revealed that the individual $\text{WO}_3\cdot\text{H}_2\text{O}$ nanosheets has an intimate contact with each other on the ITO-PET substrate, accompanying with a uniform thickness of 600 nm throughout the all area. Figure 2b shows the current versus voltage (I - V) curves of the fabricated devices as measured with a dc voltage sweeping mode. During the measurements, the voltage is applied to the top Cu electrode, and the bottom ITO/PET electrode is grounded. In the characteristic I - V curve of $\text{Cu}/\text{WO}_3\cdot\text{H}_2\text{O}$ ultrathin nanosheets/ITO-PET device (green line), starting from a high-resistance state (HRS), the current level suddenly increases at ~ 1 V to a low-resistance state (LRS). In the subsequent sweep from a positive voltage to zero, the device sustains the LRS. During the negative sweep, the current abruptly decreases at the bias voltage of -1.14 V, indicating that the device switches back to HRS. The reverse biases induced current increase and decrease define the set (ON) and reset (OFF) values, respectively, indicating typical bipolar resistive switching characteristics. The low set/reset voltage enable this device can be readout at a low-voltage bias (<1 V). A significantly high ON/OFF ratio as large as 10^5 is achieved in our $\text{WO}_3\cdot\text{H}_2\text{O}$ nanosheets-based RRAM device. This is an ultrahigh memory margin, making the periphery circuit very easy to distinguish the storage information ("1" or "0"). Notably, this low set/reset voltage and large ON/OFF ratio of the ultrathin $\text{WO}_3\cdot\text{H}_2\text{O}$ based RRAM device are much better than those of the most reported typical resistive switching inorganic materials (as seen in Figure 2c), which indicates the ultrathin $\text{WO}_3\cdot\text{H}_2\text{O}$ nanosheets should be a promising candidate for nonvolatile memory technology. To characterize the reliable nonvolatile memory characteristics of the fabricated devices, the retention and endurance of the memories was determined. As shown in Figure 2d, the retention capabilities of the HRS and LRS were obtained under a readout voltage of 0.1 V. The resistance values of both the HRS and LRS were stable without degradation over 10^5 s. At the same time the steady resistive switching characteristics over 5000 cycles with merely small fluctuations in the HRS and LRS were observed (as seen in Figure 2e), and no evident changes was detected in the I - V curves after 5000 switching cycles (as seen in Supporting Information Figure S5). Both the retention and endurance test results undoubtedly reveal that the devices are nonvolatile and can be read nondestructively.

In addition to reliable device operation, the excellent bending stability for flexible electronics is one of the most superiority of the 2D ultrathin nanosheets-based devices. Figure 2f (blue line) demonstrates the excellent flexibility of the as-fabricated ultrathin nanosheets-based device with negligible degradation of the set/reset voltage and ON/OFF ratio even after 2000 bending cycles (as seen the inset of Figure 2f). For comparison, the flexibility test of RRAM device with $\text{WO}_3\cdot\text{H}_2\text{O}$ bulk as active materials also shows here. Although the bulk-based device exhibits similar RS behavior to ultrathin nanosheets-based device before bending (see the orange line in Figure 2b), after only 100 repeated bendings, the resistive switching memory characteristics have remarkably broken down (see the magenta line in Figure 2f). The above experimental results reveal that the ultrathin nanosheets-based device possesses more flexibility than the bulk-based device. In short, the ultrathin $\text{WO}_3\cdot\text{H}_2\text{O}$ nanosheets have shown the fascinating

electrochemical and mechanical characteristics for practical applications in high performance and excellent flexible RRAM devices catering for portable and flexible electronics.

Nowadays, the switching mechanisms in RRAM are still in dispute, and the valence-change mechanism is usually thought to be responsible for the resistive switching in most metal oxides, in which the oxygen vacancy is regarded as the mobile species to cause the resistive switching through the formation and rupture of conductive filaments. The device driven by this mechanism usually shows bipolar behavior,¹⁰ in which the LRS and HRS states are switched with opposite bias polarity. In our case, the apparent bipolar behavior of the ultrathin $\text{WO}_3\cdot\text{H}_2\text{O}$ nanosheets-based RRAM device is tempting to believe that the valence-change mechanism dominates the resistive switching. However, the electron spin resonance (ESR) measurement, a well-established technique to provide fingerprint evidence for probing oxygen vacancies, clearly reveals the absence of the isolated oxygen vacancy in the as-obtained ultrathin $\text{WO}_3\cdot\text{H}_2\text{O}$ nanosheets. It is well known that the isolated oxygen vacancy usually shows the characteristic ESR signal with g value of 2.000 derived from the trapped free electrons at oxygen vacancies.³² However, in our case, no detection of this ESR confirms the absence of the isolated oxygen vacancy in our samples (as seen in Figure 3b). This fact urged us to ponder what mechanism

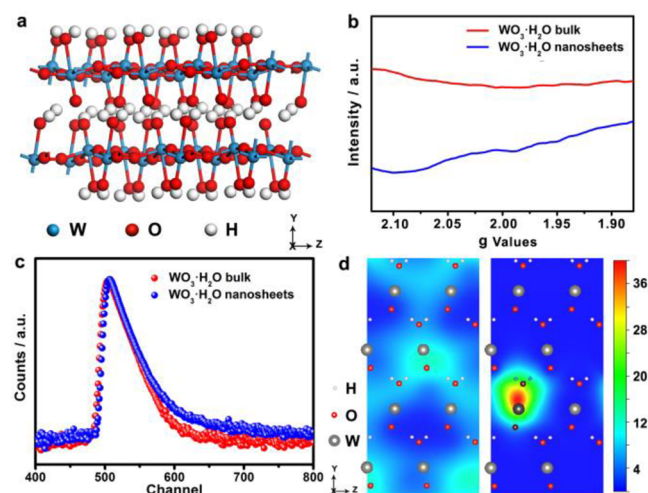


Figure 3. (a) Crystal structure of orthorhombic $\text{WO}_3\cdot\text{H}_2\text{O}$. (b) ESR spectra for as-obtained ultrathin $\text{WO}_3\cdot\text{H}_2\text{O}$ nanosheets and its bulk counterparts. No detection of g value at 2.000 ESR confirms the absence of the isolated oxygen vacancy. (c) Positron lifetime spectrum of ultrathin $\text{WO}_3\cdot\text{H}_2\text{O}$ nanosheets and its bulk counterparts. (d) Schematic representations of trapped positrons of V''' [OWOH₂] vacancy associates.

practically triggered this resistive switching in the ultrathin $\text{WO}_3\cdot\text{H}_2\text{O}$ nanosheets-based RRAM device. Of note, upon the formation of 2D materials with atomic thickness, the loss of effect in the third dimensionality inevitably induces the formation of diverse defects on the surfaces, which would play innegligible influence on their physicochemical properties. Therefore, both the identification and quantification of defects are necessary for in-depth and comprehensive understanding of origin of the higher performance of resistive switching.

Positron annihilation spectrometry is a well-established technique to determine the type and relative concentration of various defects/vacancies even at the parts per million level via measuring the lifetime of the positron.^{33,34} The positron

lifetime spectra of both $\text{WO}_3\cdot\text{H}_2\text{O}$ ultrathin nanosheets and bulk yield three lifetime components, τ_1 , τ_2 , and τ_3 , with relative intensities I_1 , I_2 , and I_3 (as seen in Table 1). The longest

Table 1. Positron Lifetime Parameters of Ultrathin $\text{WO}_3\cdot\text{H}_2\text{O}$ Nanosheets and Bulk

sample	τ_1 (ps)	τ_2 (ps)	τ_3 (ns)	I_1 (%)	I_2 (%)	I_3 (%)
nanosheets	263.2	372.8	2.48	26.4	73.3	0.3
bulk	258.5	374.9	2.14	81.6	17.6	0.8

component (τ_3) is attributed to the positron annihilation in the large voids present in the material. According to the theoretically calculated position lifetime values of $\text{WO}_3\cdot\text{H}_2\text{O}$ (as seen in Table 2), the shortest one (τ_1 , around 260 ps)

Table 2. Calculated positron lifetime values of $\text{WO}_3\cdot\text{H}_2\text{O}$

defect	bulk	$V_{[\text{OWOH}_2]}$
lifetime (ps)	265.5	373.4

observed in the experimental positron lifetime spectra could be assigned to bulk defects in the perfect crystal, whereas another component (τ_2 , around 373 ps) could be attributed to positron annihilation as trapped at vacancy associates, $V^{m+}_{[\text{OWOH}_2]}$ (Figure 3d). In addition, the relative intensity (I) gives more information on the distribution of these defects because the relative intensity can quantify the abundance of that defect with respect to some standard of the same material. It is clear that the vacancy associates concentration in $\text{WO}_3\cdot\text{H}_2\text{O}$ ultrathin nanosheets is much higher than that of bulk counterparts. Taking into account the crystal structure of $\text{WO}_3\cdot\text{H}_2\text{O}$, two type of O atoms connect to the W atoms: one type is perpendicular to the [010] direction, whereas the other is parallel to the [010] direction. The latter does not further connect to any other atoms except the isolated H atoms. As the thickness of $\text{WO}_3\cdot\text{H}_2\text{O}$ nanosheets is reduced to atomic scale, the buried internal W atoms become easier to escape from the lattice, which can simultaneously carry the parallel [010] direction O atoms and H atoms to break away the lattice. Thus, the vacancy associates in the $\text{WO}_3\cdot\text{H}_2\text{O}$ ultrathin nanosheets can form much more readily than the bulk samples, which has been verified by the result of relative intensity of positron lifetime. It is worth noting that every vacancy associate has a four negative charge bounding four holes for compensation, e.g. $[V^{m+}_{[\text{OWOH}_2]}] = 4[h^+]$, which can act as carrier reservoir to provide carriers under applied electric field, benefiting the lower energy consumption memory effect.

On the other hand, electrochemical metallization is the other common accepted mechanism to explain the resistive switching phenomena, in which the mobile species is believed to be the metallic cation. While in this mechanism-mediated RRAM device, an important signature is to have an electrode made from an electrochemically active material, such as Cu or Ag. In order to identify the origin of the high performance of our ultrathin $\text{WO}_3\cdot\text{H}_2\text{O}$ based RRAM device, we constructed PET-ITO/ $\text{WO}_3\cdot\text{H}_2\text{O}$ /ITO-PET device for comparison, in which the ITO acts as inert electrode and can not provide the activated metallic ions. Such a device with symmetric inert electrodes also shows similar bipolar RS characteristics except the higher set/reset voltages (+4.6 V/−5.0 V) and lower HRS/LRS ratio (10^4) (as seen in the Supporting Information Figure S6). As is well known, the activated metallic ions can be trapped by the

defects to form the conductive filaments.³⁵ Therefore, this result undoubtedly indicates that the active Cu electrode should play an important role in the ultrathin based RRAM device, which means the electrochemical metallization mechanism may be also responsible for the low power consumption of this device.

In order to further comprehend the switching mechanisms, we replotted the I - V characteristics in a log-log scale, which are shown in Figure 4. As shown in Figure 4a, three clearly

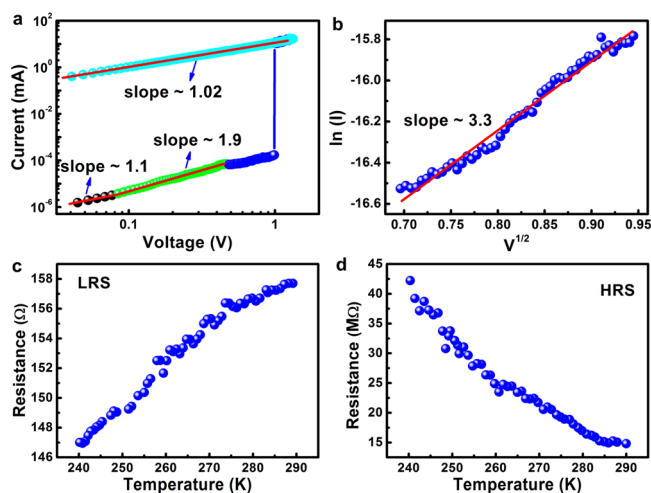


Figure 4. (a) Typical I - V curves plotted on a log-log scale. (b) Typical $\ln(I)$ vs $V^{1/2}$ plot for the higher-voltage region of the HRS. (c) and (d) Temperature dependence of the resistances for HRS and LRS, respectively.

distinguished regions were observed in the best fitted I - V characteristics for the HRS. As the voltage below 0.1 V, the I - V characteristic shows a linear relationship with a slope of 1.1 indicates that ohmic conduction is the key conduction mechanism in this range, resulting from the fact that the thermally generated carriers exceed the injected carriers. In the intermediate voltage range from 0.1 to 0.5 V, the slope of I - V characteristic increases near to 2, suggesting the dominant space-charge limited current, in which the injected carriers are partly captured by the traps energy level below the conduction band in the $\text{WO}_3\cdot\text{H}_2\text{O}$ nanosheets. As voltage further increases to above 0.5 V (as shown in Figure 4b), a linear change in the logarithmic plot of $\ln(I)$ versus $V^{1/2}$ with a slope of 3.3 was observed in the I - V characteristics of the HRS, which suggests that the Schottky emission dominates the carrier transport in the HRS. In contrast, the I - V relationship in LRS clearly exhibits an Ohmic conduction behavior, which is regarded to the formation of conductive filaments in the device during the SET process. The resistance of the LRS increased with temperature increasing also confirms the formation of metallic conductive filaments (Figure 4c), whereas the resistance of the HRS decreased with temperature increasing, indicating a semiconductive behavior in HRS (Figure 4d). For comparison, we also investigated the switching mechanism for PET-ITO/ $\text{WO}_3\cdot\text{H}_2\text{O}$ /ITO-PET device through replotted the I - V characteristics in a log-log scale, which are shown in the Supporting Information Figure S6. From the Figure S6, the different switching mechanism in inert electrode-based device implies that vacancy associates should play an important role in the active electrode-based device for the high switching performance.

On the basis of the above experimental results and theoretical analysis, a dual synergic mechanism is therefore unambiguously proposed to account for the high performance of resistive switching memory effect in the ultrathin $\text{WO}_3 \cdot \text{H}_2\text{O}$ -based RRAM device. Because the holes are limited around the vacancy associates (as seen in Figure 5), it is very difficult for

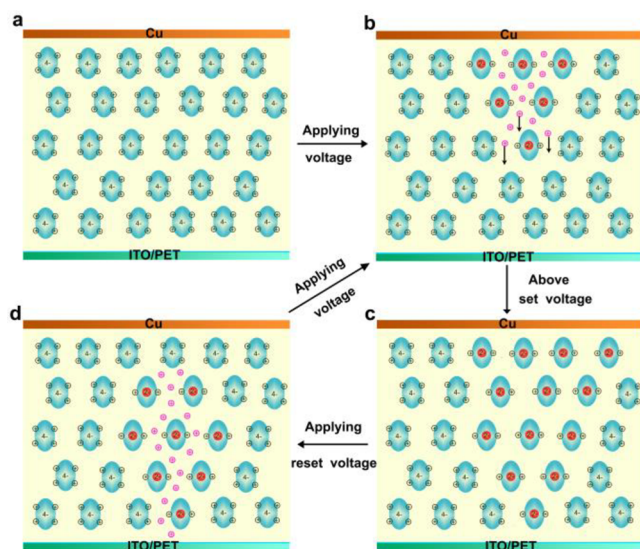


Figure 5. Big ovals represent vacancy associates, the small black circles represent the bound holes, and the small pink circles represent the free holes. (a) Initial high resistance state. (b) When the voltage is applied, Cu^{2+} injected from electrode will fill the vacancy associates position and release the excess holes, which move toward ITO/PET electrode under electric field. (c) When the applied voltage reaches the set voltage, the conductive filament will contact the anode and cathode electrodes, corresponding to a low resistance state. (d) When the reset voltage is applied, the conductive filament will be broken and the device will switch to a high resistance state.

them to move/migrate in the $\text{WO}_3 \cdot \text{H}_2\text{O}$ -based thin film, resulting that the RRAM device shows sufficiently high resistive in the OFF state. Under a positive voltage applied to the active Cu electrode, metal Cu is oxidized to form Cu^{2+} . The Cu^{2+} ions injected from electrode will first fill the vacancy associate position due to the more small resistive to form new $V''_{[\text{CuO}(\text{WOH}_2)]}$ defect, which only needs two holes to compensate the charge. Thus, the two excess holes, which was confined around the vacancy associates, will be released into the $\text{WO}_3 \cdot \text{H}_2\text{O}$ -based active layer. This injection of oxidized Cu^{2+} into active layer is also verified by XPS in the respective initial resistance states (IRS), low resistance state (LRS) in set process and high resistance state (HRS) in reset process, which were shown in the Supporting Information Figure S7. The incorporated Cu^{2+} ions can also be considered as the conductive phase, which grows toward the ITO electrode under the electric field. Once the voltage reaches a certain value, the conductive filament will contact the anode and cathode electrodes penetrate the electronic barrier, corresponding to the device switching from HRS to LRS. When the reverse voltage is applied, the Cu^{2+} ions close the cathode electrode will be first reduced to Cu and the Cu^{2+} ions concentration will gradually decrease at the electronically conducting zone close to the Cu electrode. The resistive switching from LRS to HRS is accomplished by the rupture of the conductive filament under a certain reverse voltage. In this

mechanism, the vacancy associates act not only carrier reservoir to provide carriers but also capture center to trap the activated Cu^{2+} for the formation of conductive filaments, which synergistically cause the low set/reset voltages and high HRS/LRS ratio in the $\text{WO}_3 \cdot \text{H}_2\text{O}$ -based RRAM device.

CONCLUSION

In summary, we highlight an inorganic graphene analogue, ultrathin $\text{WO}_3 \cdot \text{H}_2\text{O}$ nanosheets with only 2–3 nm thickness, as a promising material to construct a high performance and flexible RRAM device. The positron annihilation spectra clearly confirm the formation of vacancy associates in the ultrathin nanosheets as the thickness reduces to atomic level, which act not only carrier reservoir to provide carriers but also capture center to trap the activated Cu^{2+} for the formation of conductive filaments. As a result, these abundant vacancy associates endows the ultrathin nanosheets with remarkable resistive switching memory performance, including low operating voltage (+1.0 V/−1.14 V), large resistance ON/OFF ratio ($>10^5$), long retention time ($>10^5$ s), and good endurance (>5000 cycles), which is superior to its bulk counterparts and most of the reported typical resistive switching inorganic materials. In addition, this ultrathin nanosheets-based RRAM device also shows excellent flexibility due to its 2D ultrathin characteristic, which is usually difficult to achieve in both bulk and nanoparticles. The finding of the existence of distinct defects in ultrathin nanosheets undoubtedly leads to an atomic level deep understanding of the underlying nature of the resistive switching behavior, which may serve as a guide to improve the performances and promote the rapid development of RRAM.

ASSOCIATED CONTENT

Supporting Information

Characterization of bulk $\text{WO}_3 \cdot 2\text{H}_2\text{O}$; HRTEM and SAED for ultrathin $\text{WO}_3 \cdot \text{H}_2\text{O}$ nanosheets; thickness distribution; cross-sectional SEM image; repeated I – V curves after 5000 switching cycles; XPS spectra for Cu/ $\text{WO}_3 \cdot \text{H}_2\text{O}$ /ITO-PET memristor device; and resistive switching property of obtained ITO-PET/ $\text{WO}_3 \cdot \text{H}_2\text{O}$ /ITO-PET device. This material is available free of charge via the Internet at <http://pubs.acs.org>.

AUTHOR INFORMATION

Corresponding Authors

yxie@ustc.edu.cn
cxiao@ustc.edu.cn

Author Contributions

^{||}These authors contributed equally to this work.

Notes

The authors declare no competing financial interest.

ACKNOWLEDGMENTS

This work was financially supported by National Natural Science Foundation of China (21331157, 21331005, 21401182, and 91422303), National Basic Research Program of China (2015CB932302), the Fundamental Research Funds for the Central University (WK2060190020, WK2060190027), China Postdoctoral Science Foundation (No. 2014M550347), and the Opening Project of the Jiangsu Key Laboratory for Environment Functional Materials (No. SJHG1301). The authors thank Mr. Wei Liao (College of Physical Science and

Technology, Sichuan University) for his helpful discussions and suggestions.

REFERENCES

- (1) Borghetti, J.; Snider, G. S.; Kuekes, P. J.; Yang, J. J.; Stewart, D. R.; Williams, R. S. *Nature* **2010**, *464*, 873.
- (2) Yang, J. J.; Strukov, D. B.; Stewart, D. R. *Nat. Nanotechnol.* **2013**, *8*, 13.
- (3) Wuttig, M.; Yamada, N. *Nat. Mater.* **2007**, *6*, 824.
- (4) Sawa, A. *Mater. Today* **2008**, *11*, 28.
- (5) Waser, R.; Aono, M. *Nat. Mater.* **2007**, *6*, 833.
- (6) Lee, M.-J.; Lee, C. B.; Lee, D.; Lee, S. R.; Chang, M.; Hur, J. H.; Kim, Y.-B.; Kim, C.-J.; Seo, D. H.; Seo, S.; Chung, U.-I.; Yoo, I.-K.; Kim, K. *Nat. Mater.* **2011**, *10*, 625.
- (7) Linn, E.; Rosezin, R.; Kugeler, C.; Waser, R. *Nat. Mater.* **2010**, *9*, 403.
- (8) Szot, K.; Speier, W.; Bihlmayer, G.; Waser, R. *Nat. Mater.* **2006**, *5*, 312.
- (9) Yang, J. J.; Pickett, M. D.; Li, X.; Ohlberg, D. A. A.; Stewart, D. R.; Williams, R. S. *Nat. Nanotechnol.* **2008**, *3*, 429.
- (10) Kwon, D.-H.; Kim, K. M.; Jang, J. H.; Jeon, J. M.; Lee, M. H.; Kim, G. H.; Li, X. S.; Park, G.-S.; Lee, B.; Han, S.; Kim, M.; Hwang, C. S. *Nat. Nanotechnol.* **2010**, *5*, 148.
- (11) Yang, Y.; Gao, P.; Gaba, S.; Chang, T.; Pan, X.; Lu, W. *Nat. Commun.* **2012**, *3*, 732.
- (12) Ji, Y.; Zeigler, D. F.; Lee, D. S.; Choi, H.; Jen, A. K.-Y.; Ko, H. C.; Kim, T.-W. *Nat. Commun.* **2013**, *4*, 2707.
- (13) Choi, M. S.; Lee, G.-H.; Yu, Y.-J.; Lee, D.-Y.; Lee, S. H.; Kim, P.; Hone, J.; Yoo, W. J. *Nat. Commun.* **2013**, *4*, 1624.
- (14) Han, S.-T.; Zhou, Y.; Roy, V. A. L. *Adv. Mater.* **2013**, *25*, 5425.
- (15) Jang, J.; Pan, F.; Braam, K.; Subramanian, V. *Adv. Mater.* **2012**, *24*, 3573.
- (16) Kim, S.; Jeong, H. Y.; Kim, S. K.; Choi, S.-Y.; Lee, K. J. *Nano Lett.* **2011**, *11*, 5438.
- (17) El-Kady, M. F.; Strong, V.; Dubin, S.; Kaner, R. B. *Science* **2012**, *335*, 1326.
- (18) Bae, S.; Kim, H.; Lee, Y.; Xu, X.; Park, J.-S.; Zheng, Y.; Balakrishnan, J.; Lei, T.; Kim, H. R.; Song, Y. I.; Kim, Y.-J.; Kim, K. S.; Özyilmaz, B.; Ahn, J.-H.; Hong, B. H.; Iijima, S. *Nat. Nanotechnol.* **2010**, *5*, 574.
- (19) Georgiou, T.; Jalil, R.; Belle, B. D.; Britnell, L.; Gorbachev, R. V.; Morozov, S. V.; Kim, Y.-J.; Gholinia, A.; Haigh, S. J.; Makarovskiy, O.; Eaves, L.; Ponomarenko, L. A.; Geim, A. K.; Novoselov, K. S.; Mishchenko, A. *Nat. Nanotechnol.* **2013**, *8*, 100.
- (20) Yang, R.; Terabe, K.; Tsuruoka, T.; Hasegawa, T.; Aono, M. *Appl. Phys. Lett.* **2012**, *100*, 231603.
- (21) Wu, W.-T.; Wu, J.-J.; Chen, J.-S. *ACS Appl. Mater. Interfaces* **2011**, *3*, 2616.
- (22) Kalantar-zadeh, K.; Vijayaraghavan, A.; Ham, M.-H.; Zheng, H.; Breedon, M.; Strano, M. S. *Chem. Mater.* **2010**, *22*, 5660.
- (23) Zheng, H. D.; Ou, J. Z.; Strano, M. S.; Kaner, R. B.; Mitchell, A.; Kalantar-zadeh, K. *Adv. Funct. Mater.* **2011**, *21*, 2175.
- (24) Boroński, E.; Nieminen, R. M. *Phys. Rev. B* **1986**, *34*, 3820.
- (25) Perdew, J. P.; Burke, K.; Ernzerhof, M. *Phys. Rev. Lett.* **1996**, *77*, 3865.
- (26) Barbiellini, B.; Puska, M. J.; Korhonen, T.; Harju, A.; Torsti, T.; Nieminen, R. M. *Phys. Rev. B* **1996**, *53*, 3820.
- (27) Oka, K.; Yanagida, T.; Nagashima, K.; Tanaka, H.; Kawai, T. *J. Am. Chem. Soc.* **2009**, *131*, 3434.
- (28) Ko, Y.; Baek, H.; Kim, Y.; Yoon, M.; Cho, J. *ACS Nano* **2013**, *7*, 143.
- (29) Hwang, S. K.; Lee, J. M.; Kim, S.; Park, J. S.; Park, H. I.; Ahn, C. W.; Lee, K. J.; Lee, T.; Kim, S. O. *Nano Lett.* **2012**, *12*, 2217.
- (30) Jeong, H. Y.; Kim, J. Y.; Kim, J. W.; Hwang, J. O.; Kim, J.-E.; Lee, J. Y.; Yoon, T. H.; Cho, B. J.; Kim, S. O.; Ruoff, R. S.; Choi, S.-Y. *Nano Lett.* **2010**, *10*, 4381.
- (31) Nagashima, K.; Yanagida, T.; Oka, K.; Taniguchi, M.; Kawai, T.; Kim, J.-S.; Park, B. H. *Nano Lett.* **2010**, *10*, 1359.
- (32) Gordon, T. R.; Cargnello, M.; Paik, T.; Mangolini, F.; Weber, R. T.; Fornasiero, P.; Murray, C. B. *J. Am. Chem. Soc.* **2012**, *134*, 6751.
- (33) Xiao, C.; Qin, X. M.; Zhang, J.; An, R.; Xu, J.; Li, K.; Cao, B. X.; Yang, J. L.; Ye, B. J.; Xie, Y. *J. Am. Chem. Soc.* **2012**, *134*, 18460.
- (34) Guan, M. L.; Xiao, C.; Zhang, J.; Fan, S. J.; An, R.; Cheng, Q. M.; Xie, J. F.; Zhou, M.; Ye, B. J.; Xie, Y. *J. Am. Chem. Soc.* **2013**, *135*, 10411.
- (35) Wang, H.; VMeng, F. B.; Cai, Y. R.; Zheng, L. Y.; Li, Y. G.; Liu, Y. J.; Jiang, Y. Y.; Wang, X. T.; Chen, X. D. *Adv. Mater.* **2013**, *25*, 5498.